

## Article

# Experimental Investigation on the Dynamic Mechanical Properties and Microstructure Deterioration of Steel Fiber Reinforced Concrete Subjected to Freeze–Thaw Cycles

Yang Li <sup>1,\*</sup>, Qirui Zhang <sup>1</sup>, Ruijun Wang <sup>1</sup>, Xiaobin Xiong <sup>1</sup>, Yan Li <sup>1</sup> and Jiayu Wang <sup>2</sup>

<sup>1</sup> State Key Laboratory of Eco-Hydraulics in Northwest Arid Region, Xi'an University of Technology, Xi'an 710048, China

<sup>2</sup> State Grid Gansu Electric Power Company, Lanzhou 730030, China

\* Correspondence: ly1990120311@163.com

**Abstract:** In this study, the dynamic mechanical properties of steel fiber reinforced concrete under the influence of freeze–thaw cycles were studied. The studied parameters include steel fiber content (0%, 1% and 2%), confining pressures (0, 5 and 10 MPa) and strain rates ( $10^{-5}$ /s,  $10^{-4}$ /s,  $10^{-3}$ /s and  $10^{-2}$ /s). Performance was also evaluated, including triaxial compressive strength, peak strain, the relationship between stress and strain, failure mode and microstructure. The results show that with the increase in F–T cycles, the compressive strength and energy absorption capacity of concrete gradually decrease. The mechanical properties of concrete increased with the addition of steel fibers during F–T cycles, and the optimum amount of steel fiber to enhance resistance to F–T cycles is 1% within the evaluation range. In this study, the effects of strain rate and confining pressure on the strength and failure mode of concrete after fiber addition are studied. Both the dynamic increase factor and the concrete strength increase linearly with the increase of strain rate, the dynamic increase factor is characterized by an increase in intensity caused by strain rate. When there is no confining, the crack direction of the concrete specimen is parallel to the stress loading direction, and when there is confining, it is manifested as oblique shear failure. The results of scanning electron microscopy analysis of the microstructure demonstrate the performance results at the macroscopic level (compressive strength and peak strain).

**Keywords:** steel fiber; concrete; strain rate; confining pressures; freeze–thaw cycle; microstructure



**Citation:** Li, Y.; Zhang, Q.; Wang, R.; Xiong, X.; Li, Y.; Wang, J. Experimental Investigation on the Dynamic Mechanical Properties and Microstructure Deterioration of Steel Fiber Reinforced Concrete Subjected to Freeze–Thaw Cycles. *Buildings* **2022**, *12*, 2170. <https://doi.org/10.3390/buildings12122170>

Academic Editor:  
Andreas Lampropoulos

Received: 26 October 2022  
Accepted: 6 December 2022  
Published: 8 December 2022

**Publisher's Note:** MDPI stays neutral with regard to jurisdictional claims in published maps and institutional affiliations.



**Copyright:** © 2022 by the authors. Licensee MDPI, Basel, Switzerland. This article is an open access article distributed under the terms and conditions of the Creative Commons Attribution (CC BY) license (<https://creativecommons.org/licenses/by/4.0/>).

## 1. Introduction

Concrete has become one of the most widely used building materials in the world, but it still has some shortcomings that limit its application in some extreme environments. Due to the complexity of its structure and use in the environment, ordinary concrete no longer fulfils the requirements of high-rise buildings, bridges and water conservancy projects [1]. Concrete deterioration caused by frost (freeze–thaw cycles) is an important issue for the service life of concrete structures in cold climates. Freeze–thaw resistance is an important indicator for the durability of hydraulic concrete. In cold regions, especially in western China, the deterioration of concrete properties caused by freeze–thaw cycles and dynamic loads such as rockfall and earthquakes seriously affects the function and long-term safety of structures. Various treatments, such as adding discontinuous fibers, using continuous fabric reinforcement materials and applying fiber-reinforced polymer for external reinforcement, have been developed to overcome these shortcomings [2]. By enhancing the tensile capacity, hardness, and durability of regular concrete, fiber reinforced concrete can significantly reduce its intrinsic fragility [3]. Steel fiber is one of the most common fibers to improve the performance of concrete [4].

The mechanical performance of concrete is somewhat affected by the quantity of steel fiber additive [5–7]. In their research on the effects of steel fibers of various lengths and

diameters on the mechanical performance of concrete, Vairagade et al. [5] and Abbas et al. [6] discovered that the compressive and tensile strengths of specimens also increase by about 10–25% and 31–47%, respectively, as the water–cement ratio rises during the addition of steel fiber. As the steel fiber content increased (0.5–1.5%), the flexural strength of the samples increased from 3% to 124% at a low aspect ratio of 65 and even up to 140% at a high aspect ratio of 80. However, Wang et al. [7] showed that when the aspect ratio is greater than 60, the ductility of concrete increases with steel fiber addition, but the strength has the opposite results. Farhan et al. [8] revealed that compared with ordinary concrete, steel fiber reinforced concrete (SFRC) has a 30% higher splitting tensile strength and flexural strength. According to Yoo et al. [9], SFRC has higher ductility and strain capacity than ordinary concrete, and the least amount of fiber required to noticeably enhance flexural properties of concrete is 1%. The high compressive strength is associated with the poor ductility of the bending member. According to Yang et al. [10], the addition of fibers enhances ductility to meet the appropriate response of the structure to dynamic loads. Zhang et al. [11] proposed that the addition of fibers improves the impact resistance of concrete. In addition, Kantar et al. [12] proposed that fibers could inhibit the dynamic cracking of concrete matrix.

Numerous works have evaluated the dynamic mechanical characteristics of SFRC, particularly under uniaxial compression state [13–17]. Several studies have shown that steel fibers can enhance the dynamic mechanical properties of concrete [18–20]. According to Farhan et al. [13], the fiber content of SFRC beams has less impact on their elastic modulus and compressive strength, whereas peak strain and mechanical behavior after cracking are greatly affected. Zhang et al. [15] tested the dynamic compression properties of hybrid fiber ultra-high toughness cement matrix composites. Generally, energy absorption is closely related to steel fiber content, and the strain rate sensitivity of dynamic compressive strength rises as the steel fiber content increases. Zhang et al. [17] pointed out that the rate of increase in energy absorption was higher than the rate of increase in strength and strain as the strain rate or fiber content increased. As steel fiber is added when the strain rate is high, the damage of SFRC is reduced. The dynamic elastic modulus and peak strain are unaffected by the content and kind of steel fiber, according to Ren et al. [20], and the dynamic compressive strength is only marginally increased. Straight steel fiber has a slightly better impact on dynamic compressive strength than hook end steel fiber at a steel fiber volume content of 2.0%. Similar conclusions were drawn from previous studies [14,16]. For example, the micro straight steel fiber has better dynamic compressive strength enhancement effect than twisted steel fiber [14]. Additionally, Wu et al. [16] reported that in terms of enhancing the dynamic tensile strength, 1% straight steel fiber performs better than hook end steel fiber with the same content.

SFRC often works under multi-axial stress under dynamic loads with different strain rates, and in actual engineering, the confining pressure of different parts has a significant impact on the failure mode of concrete [21–25]. To study the triaxial behavior of steel fiber reinforced cementitious mortar, Noori et al. [23] performed a compressive experiment with various confining pressures (0–20 MPa). The findings demonstrate that the ability to absorb energy of steel fiber reinforced cementitious mortar is enhanced by the addition of steel fibers, and that the peak triaxial stress and strain are nonlinearly related to the confining pressure. Li. et al. [22] investigated the multi-axial response of high-performance fiber-reinforced cement composites and suggested that the effect of fiber content in compression and tension tests is small for the considered range from 1% to 2% and the restraint effect provided by fibers is minor in triaxial compression tests. Foltz et al. [24] evaluated the biaxial behavior of high-performance fiber-reinforced cement composites and found that its biaxial compression property is enhanced by fibers. However, Lu and Thoms [21] discovered that the nonlinear stress–strain relationship of high-strength concrete is barely impacted by steel fiber during triaxial compression, and high-strength concrete and steel fiber high-strength concrete are basically in the same ultimate strength envelope under Mohr Coulomb and Willam–Warnke failure criteria. The impacts of steel fiber and strain rate on the dynamic compressive behavior of SFRC as well as its dynamic compressive

strength, dynamic influence factor, dynamic strength criterion and failure mode were examined by Bao et al. [25]. In general, the failure mode is strongly associated with confining pressure, and the dynamic compressive strength of SFRC is favorably correlated with strain rate.

In addition, many SFRC structures are also affected by freeze–thaw (F–T) damage [26–28]. The F–T cycle is one of the essential factors causing damage to SFRC structure [29–31]. Systematic tests by Miao et al. [29] and Liu et al. [26] have shown that steel fiber addition is able to suppress the dynamic modulus loss of concrete. SFRCs were put through F–T cycles in water and NaCl solutions, and Niu et al. [30] looked at how they performed. They came to the conclusion that using steel fibers improved the pore structure with relatively minimal damage to concrete. The deterioration degree of the concrete under the F–T cycle is greatly reduced at a 1.5% steel fiber content. This finding does not coincide with the study by Zhang et al. [27], who found there was a minimal influence on the mass loss of concrete with 1.5% steel fiber under salt freezing. Wang and Niu [28] studied the performance of shotcrete containing steel fiber after a F–T cycle and sulfate erosion and found that steel fiber could form relatively compact microstructure in the matrix of shotcrete, reduce the loss of tensile stress and lead to an increase in early compressive strength and splitting strength. In addition, the best frost and sulfate resistance is found in steel fiber-reinforced shotcrete. Wang et al. [31] investigated the mutual coupling action of fiber addition and F–T cycles on impact resistance performance of SFRC using the digital image method. Therefore, it is crucial to comprehend the response of SFRC after F–T cycles under dynamic loads for the logical design and objective scientific study of structures.

As can be seen from the above literature review [26–31], although there have been some experimental studies on SFRC under freeze–thaw cycles, most of these studies have focused on the dynamic behavior under uniaxial compression. The limited available studies focus on the multiaxial performance of SFRC, especially after F–T cycling. Although the experimental research on the dynamic characteristics of SFRC under uniaxial compression has been relatively perfect, there is still a lack of research on the degradation of the dynamic performance of SFRC under F–T impact under triaxial compressive stress.

The objective of this study is to investigate the dynamic mechanical characteristics of the SFRC after F–T impact at different confining pressures (0, 5 and 10 MPa) and strain rates ( $10^{-5}/s$ ,  $10^{-4}/s$ ,  $10^{-3}/s$  and  $10^{-2}/s$ ). To determine the impact of steel fiber content, strain rate, F–T cycle and confining pressure on dynamic compressive properties, such as triaxial compressive strength, peak strain, stress–strain behavior, failure mode and dynamic increase factor (DIF), which was introduced to further understand the enhancement of dynamic compressive strength, SFRC specimens with three steel fiber contents (0 to 2% by volume) were tested under dynamic triaxial servo-hydraulic testing equipment. Finally, the microstructural feature of SFRC under F–T cycles was investigated via scanning electron microscopy (SEM).

## 2. Experimental Program

### 2.1. Materials

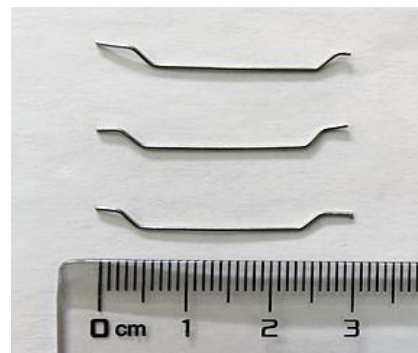
This test used ordinary Portland cement (P.O.42.5) of Chinese standard (GB 175-2007) [32], and Table 1 provides information on the chemical makeup of cement. The continuous gradation of 5–20 mm is used, with a maximum particle size of 20 mm for the coarse aggregate. River sand with a fineness modulus of 2.35 constitutes a fine aggregate. According to the related literature [8,10,13], the three gradients of steel fiber were selected. Table 2 displays information on the characteristics of aggregate. The morphology of the steel fiber used in the test is shown in Figure 1, and their performance characteristics and characteristics are shown in Table 3. The volume fractions of steel fiber are 0%, 1.0% and 2.0%. Polycarboxylate superplasticizer was used in the test. The concrete mixture proportions are shown in Table 4.

**Table 1.** Chemical composition of the cement.

Contents	Cement
SiO <sub>2</sub> (%)	21.45
Al <sub>2</sub> O <sub>3</sub> (%)	6.45
CaO (%)	61.5
Fe <sub>2</sub> O <sub>3</sub> (%)	3.09
MgO (%)	1.21
K <sub>2</sub> O (%)	1.38
Na <sub>2</sub> O (%)	0.25
SO <sub>3</sub> (%)	2.01
Loss on ignition (%)	4.05
Specific gravity (g/cm <sup>3</sup> )	3.15

**Table 2.** Properties of aggregates.

Properties	Natural Sand	Coarse Aggregate
Water absorption (%)	0.79	0.76
Loose bulk density (kg/m <sup>3</sup> )	1678	1430

**Figure 1.** Steel fiber used in this test.**Table 3.** Properties of steel fiber.

Length (mm)	Diameter (mm)	Aspect Ratio (l/d)	Elastic Modulus (GPa)	Tensile Strength (MPa)	Density (kg/m <sup>3</sup> )
30	0.5	60	200	1195	7.85

**Table 4.** Mixture proportions of concrete (kg/m<sup>3</sup>).

Specimens ID *	Water	Cement	Sand	Coarse Aggregate	SUPERPLASTICIZER	Steel Fibers
SF0	150	375	765	1135	2.63	0
SF10	150	375	730	1095	2.63	78
SF20	150	375	710	1045	2.63	156

\* Note: For example, the specimen ID of SF10 denotes that the specimen with 1.0% steel fiber.

## 2.2. Experimental Methods

To evaluate the triaxial compressive strength of SFRC, in accordance with the standard (CECS 13:2009) [33], several cylindrical specimens with a diameter of 100 mm and a height of 148 mm of 200 mm were made. In order to ensure the uniform distribution of steel fibers, the mixing method is shown in Figure 2. The test piece was cast in a steel mold, removed from the mold after 24 h, and then allowed to cure for 28 days at a temperature of (20 ±

2) °C and a relative humidity of at 95%. Three samples were used for each test, and the outcomes were averaged.

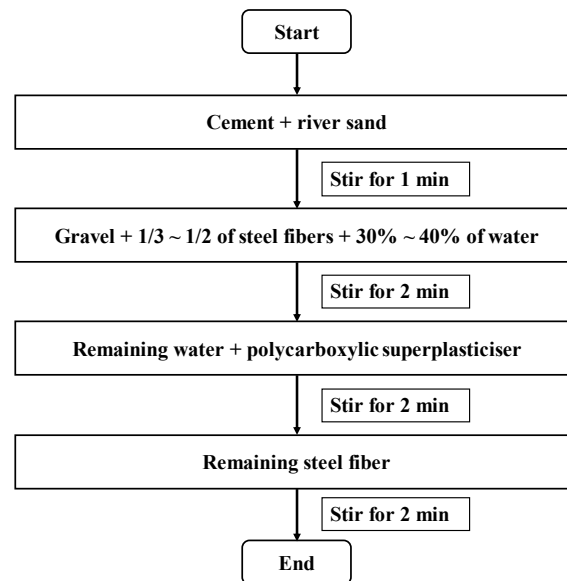


**Figure 2.** Mix procedures.

The dynamic mechanical properties of SFRC were tested on a triaxial testing system as shown in Figure 3. The axial load capacity is 2000 KN for concrete materials, and its precision is 0.1%. The specific operation of this triaxial test is divided into the following four steps: (I) Install the concrete specimen. First, place the filter paper and the permeable gasket on the base of the instrument, and place the steel fiber reinforced concrete specimen that has reached the curing age on the test instrument, and then place another gasket on its upper part. (II) Debug the displacement sensor. First, connect the displacement sensor to the triaxial tester, then enter the software control page, and slowly adjust the position of the sensor until the page shows that the displacement is zero or near zero. (III) The specimen enters the test station. Manually control the pressure cylinder so that it completely covers the test piece, and securely clamp the clamping groove to the pressure cylinder and the base of the instrument. (IV) When ready, the axial load from the compressor is applied via displacement control to start the test at a constant loading rate of 0.1 mm/s. Once a transverse deformation reaches 2 mm, that is, the deformation limit of the biaxial loading device to maintain its elastic properties, the loading is terminated.

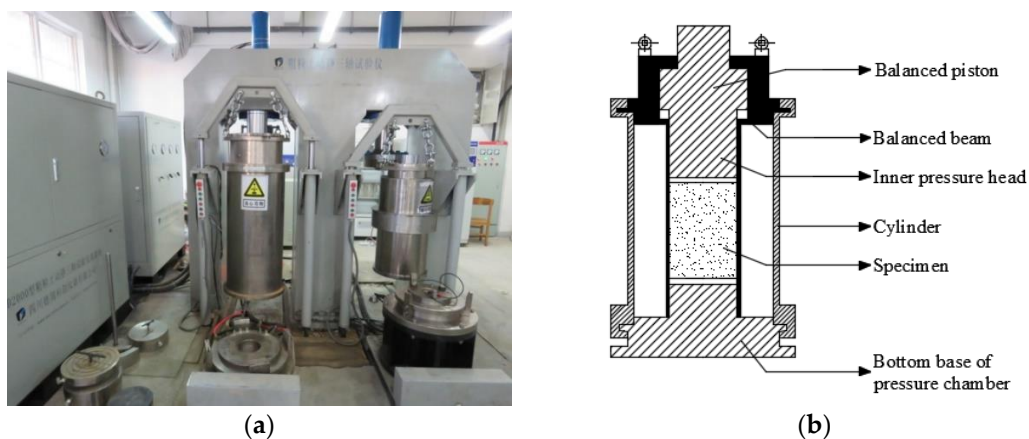


**Figure 3.** Test setup: (a) servo-hydraulic static and dynamic triaxial testing system; (b) schematic of the system.

According to the requirements of GB/T 50082-2009 [34], the F–T experimental process was designed, and the fast cycle F–T testing machine was adopted. The temperature range is controlled from 5 °C to –18 °C. A full F–T cycle is 4 h, and the number of freeze–thaw cycles was set to 0, 50, 100, 150 and 200 times. During the F–T cycle, the specimen is placed in a rubber box filled with water. The liquid with high specific heat capacity (75 wt.% ethylene glycol) flows in a circular manner in the shape of a rubber box, which enables the freeze–thaw of water and specimens. According to the concrete mix ratio in Table 4, several cylindrical specimens with a diameter of 100 mm and a height of 200 mm were produced. The specimens were subjected to triaxial compression tests under different steel fiber content (0%, 1% and 2%), confining pressure (0, 5 and 10 MPa), and strain rate ( $10^{-5}/s$ ,  $10^{-4}/s$ ,  $10^{-3}/s$  and  $10^{-2}/s$ ).

The mechanical properties test of concrete specimens obtained the triaxial compressive strength, peak strain and axial compressive stress–strain curves of concrete specimens at various confining pressures and strain rates. To determine the test pieces' failure mode, the appearance changes for the test pieces that finished the experiment were recorded.

The microstructure of the samples was analyzed by SEM. The specific operation is divided into the following four steps: (I) Select a small concrete block with a size of about 5 mm × 5 mm × 5 mm from the steel fiber reinforced concrete specimen after triaxial compression failure, as shown in Figure 4, and ensure that its section is flat. (II) After immersing the sample in absolute ethanol for 24 h, remove it out and dry it. (III) After the drying is completed, remove the dust on the surface of the sample, and then start to spray gold to improve its conductivity, which is conducive to the observation of the appearance. (IV) Place it into the electron microscope scanner for observation.

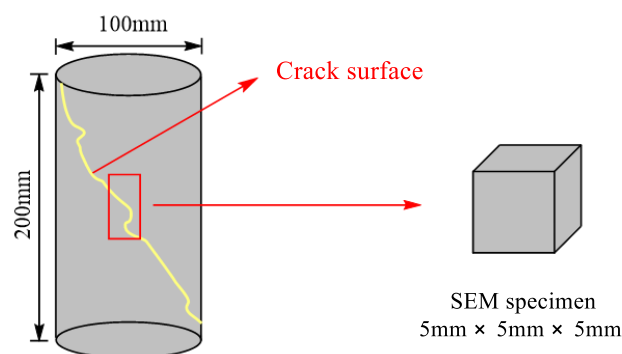


Figure 4. Schematic of the preparation of the specimen for SEM test.

### 3. Results and Discussion

#### 3.1. Triaxial Compressive Strength

Selected specimens were frozen and thawed 0, 50, 100, 150 and 200 times to determine the impacts of the F–T cycles on the dynamic performance of concrete. The compressive strength of specimens at a 5 MPa confining pressure without F–T cycles is shown in Figure 5. It is different from what can be observed; the compressive strength rises as the strain rate rises. Additionally, the compressive strength is somewhat improved by the steel fiber. At a  $10^{-5}/s$  strain rate, the compressive strength of the specimens with 0%, 1% and 2% steel fiber are 66.34 MPa, 68.15 MPa and 67.03 MPa, respectively. The specific reasons are analyzed below. The relative compressive strength of specimens with a 5 MPa confining pressure at various F–T cycles is shown in Figure 6. It is evident that as the number of F–T cycles rises, the compressive strength of concrete gradually decreases. Lu et al. [35] reported similar outcomes. The decrease in the compressive strength of concrete is due to the fact that the pore solution in the concrete undergoes repeated freeze–thaw processes after each F–T cycle and causes expanding internal cracks, surface fouling and loss of overlay thickness, and adding fibers to a concrete sample can reduce the number of cracks and increase strength [30,31]. Furthermore, concrete specimens that were subjected to F–T

cycles showed the following two stages in their triaxial compressive strength: (I) a slow decline phase from the start of F–T cycles to 50 F–T cycles, and (II) an accelerated descent stage from 50 F–T cycles. As an illustration, the triaxial compressive strength of the concrete specimen SF0 with a strain rate of  $10^{-5}/s$  fell by 4.7% and 40.5% after 50 and 200 F–T cycles, respectively. The gradual decline in the triaxial compressive strength may be due to a gradual loosening of the aggregate and mortar of the concrete specimen and internal structure as the number of cycles increases.

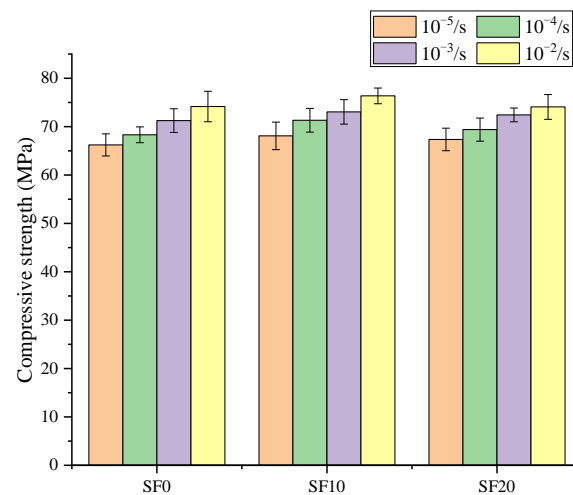


**Figure 5.** Compressive strength of concrete specimens with 5 MPa confining pressure without F–T cycles.

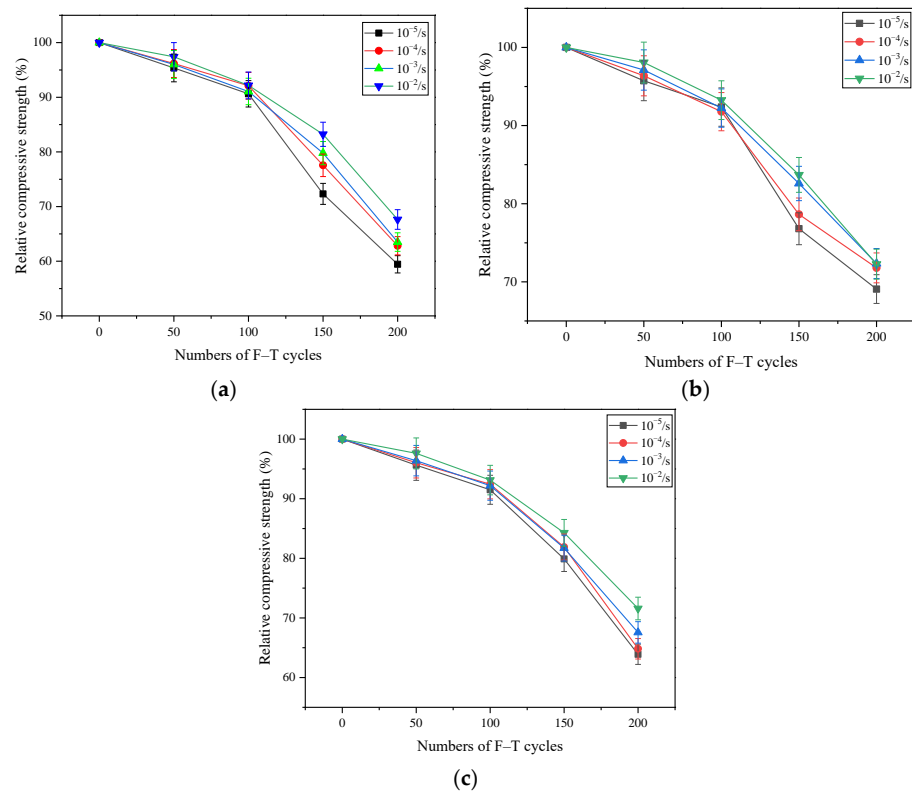


**Figure 6.** Relative compressive strength of concrete specimens with 5 MPa confining pressure under different numbers of F–T cycles. (a) SF0, (b) SF10 and (c) SF20.

The triaxial compressive strength of all mixes subjected to F–T cycling exhibits the clear phenomena of rising with increasing strain rate, this result is in accordance with

previous research [35–37]. Triaxial compressive strength may have increased for two causes: (I) when the strain rate is great, the crack growth rate is fast, the number is large and the area of the region increases. As a result, a lot of energy is required for fracture development, and the concrete does not have enough time to store and collect energy. The only way to increase the extra energy is to put more pressure on the loading point, and the ultimate performance is the increase in material strength [38]; (II) according to the description of the Stefan effect, viscous fluid exists between two solid parallel plates at a distance. When two plates are separated or approached at a certain speed, the viscous resistance produced by the viscous fluid has an impact on how quickly the plates move, which is positively related to the speed of the plates, as shown in Figure 7. Given that the macro cracks of concrete materials are hindered by the viscous effect during expansion, a high strain rate will lead to a great viscous effect and the improvement of concrete strength [39–41]. This explains why compressive strength increases with the rate of strain.

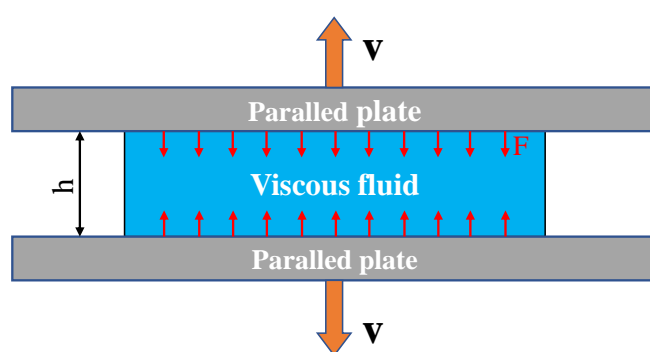
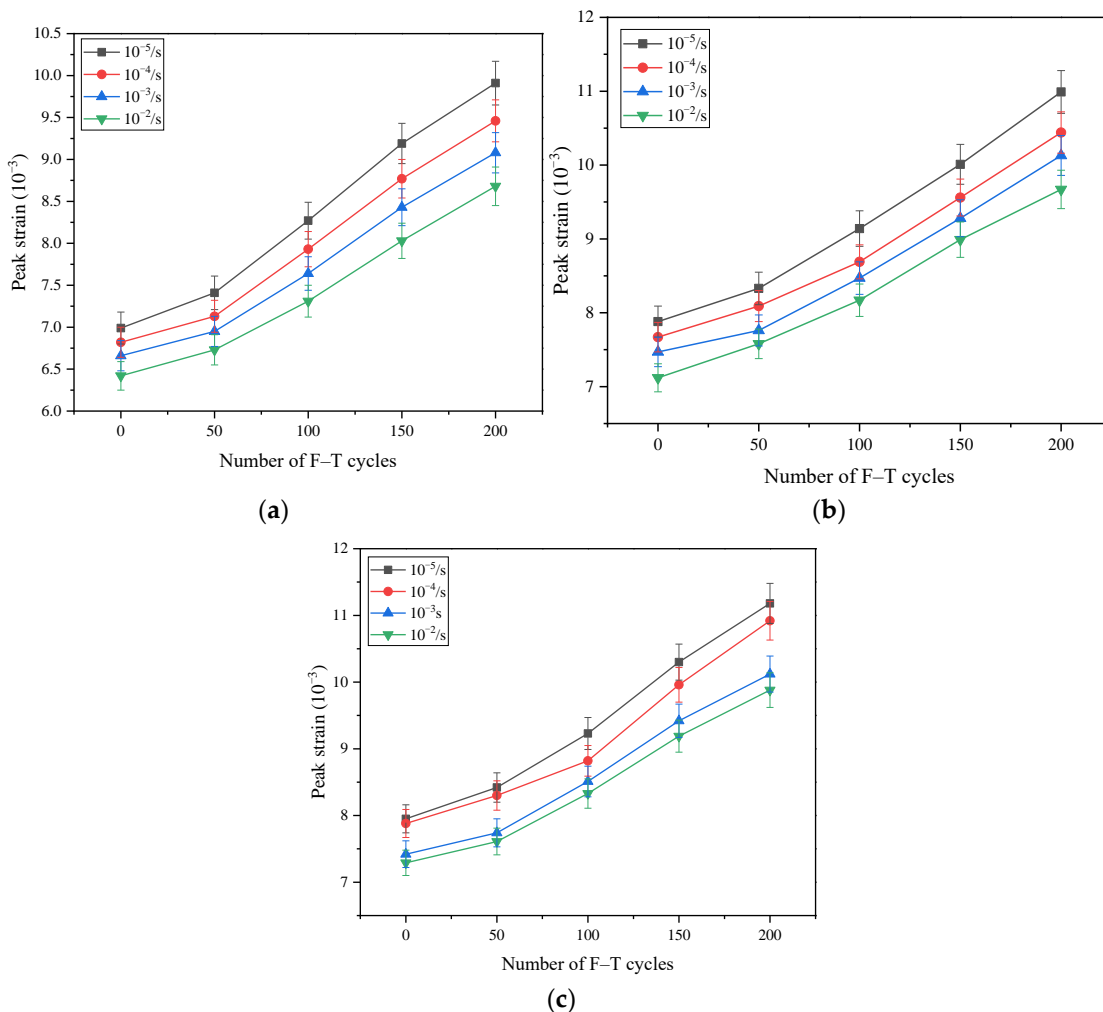


Figure 7. Stefan effect.

The addition of steel fiber to concrete increases its ultimate triaxial compressive strength. Zhang et al. [19] and Han et al. [42] noted that decreasing the average gap between fibers can be accomplished by adding more steel fiber in the right amounts; hence, the majority of the fibers will bear the load. The stress between fiber and matrix decreases with the increase in fiber content, thereby delaying the formation and propagation of cracks. The strength of SFRC showed a certain downward trend as the steel fiber percentage reached 2.0%. This is because excessive steel fiber causes a small amount of agglomeration, resulting in a ‘balling effect’ in concrete [43]. Additionally, the concrete slurry becomes insufficient, which thus reduces the filling and wrapping effect.

### 3.2. Peak Strain

The influence of F–T cycle number on the axial peak strain of concrete specimens at a 5 MP confining pressure and different strain rate is shown in Figure 8. It is evident that the axial peak strain of the specimens increases as F–T cycles increase. Take a strain rate of  $10^{-5}/s$  as an example, the axial peak strain increases by 42.1%, 39.3% and 40.5% for SF0, SF10 and SF20, respectively, from 0 F–T to 200 F–T cycles. This result is analogous to that of Zhao et al. [31], who discovered that the F–T cycles damage the concrete and therefore reduce its dynamic performance, thereby leading to concrete deformation after F–T to a large degree under the same energy. Additionally, it can be found that peak strain of the specimens subjected to F–T cycles is similar to compressive strength which exhibits following two phases: (I) there is a gradual increase phase from the first immersion through 50 F–T cycles and (II) an accelerating increase phase from 50 to 200 F–T cycles.



**Figure 8.** Peak strain of concrete specimens with 5 MPa confining pressure under different number of F-T cycles. (a) SF0, (b) SF10 and (c) SF20.

The axial peak strain of all concrete after 100 F-T cycles is shown in Figure 9. All mixtures share an obvious feature in that increasing the strain rate consistently reduces the axial peak strain. For SF0, when the confining pressure is 0 MPa, the axial peak strain (Figure 9a) under the strain rate of 10<sup>-4</sup>/s, 10<sup>-3</sup>/s and 10<sup>-2</sup>/s are decreased by 4.4%, 8.0% and 10.6%, respectively, compared with that under the strain rate of 10<sup>-5</sup>/s. As a result, with the same number of F-T cycles, the axial peak strain of concrete specimens without steel fiber falls as the strain rate increases. Figure 9b, c reveal that the concrete with 1% and 2% steel fiber shows a similar trend.

Figure 9 displays the impact of confining pressure on the axial peak strain of all mixes. The axial peak strain of all concrete showed a continuous increasing trend with increasing confining pressure. When the confining pressure is increased from 0 to 10 MPa for SF0, the axial peak strain (Figure 9a) rises by 98.0% at a 10<sup>-5</sup>/s strain rate. Furthermore, for SF10 at a 10<sup>-5</sup>/s strain rate, the axial peak strain (Figure 9b) increased from 0.0057 to 0.0113 with the strain rate was raised from 0 MPa to 10 MPa. For concrete with 2% steel fibers (SF20), the results are consistent with those for SF0 and SF10 shown in Figure 9c. This result is in line with research by Wang et al. [44], who found that the peak strain of the specimen rises with increasing confining pressure.

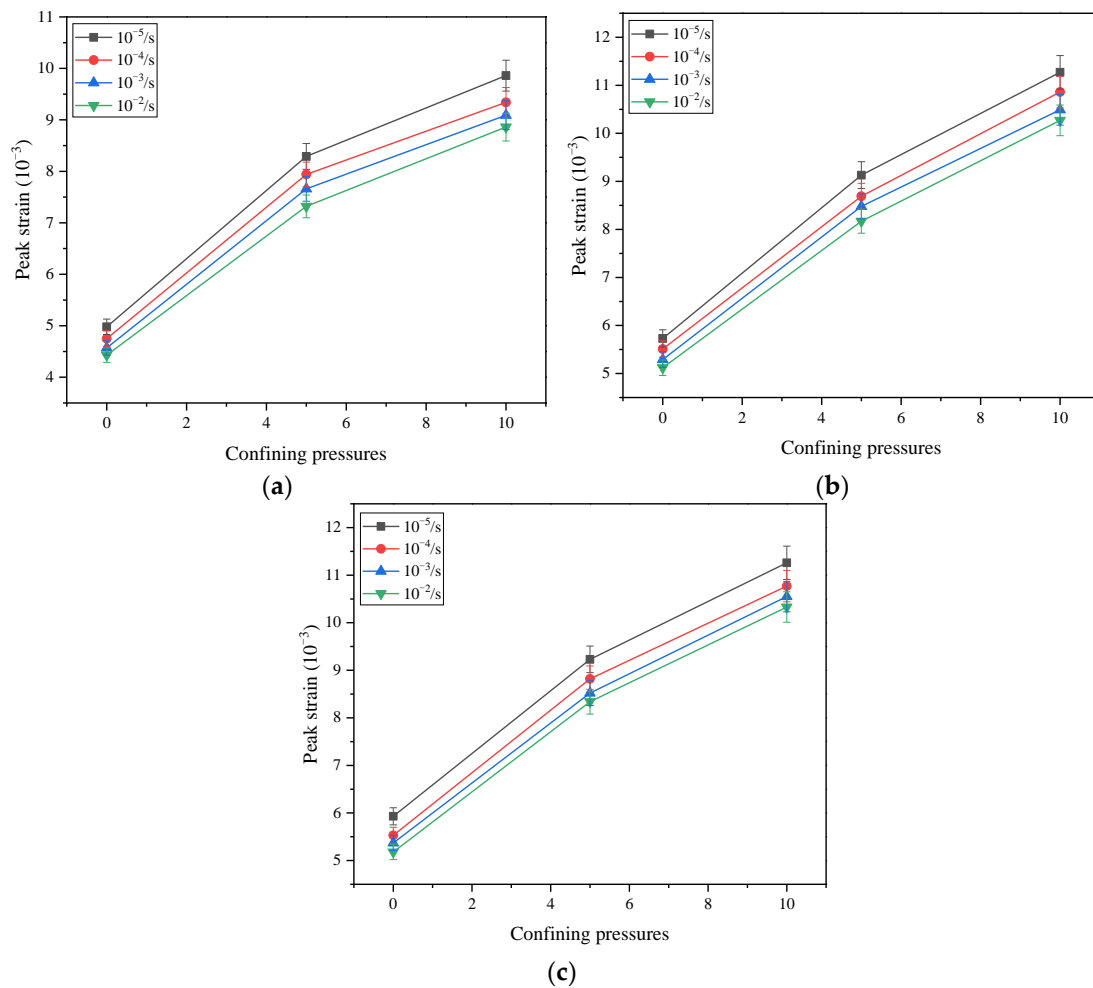


**Figure 9.** Peak strain of concrete specimens with 100 F–T cycles under different confining pressures. (a) SF0. (b) SF10. (c) SF20.

Furthermore, Figure 9 demonstrates that adding steel fiber in the test will increase the axial peak strain of concrete. When the confining pressure is 0 MPa, for instance, the peak strain of SF10 and SF20 increases by 14.9% and 19.1%, respectively, over that of SF0 at a  $10^{-5}/s$  strain rate.

### 3.3. Axial Stress–Strain Behavior

The influence of F–T cycle number on the stress–strain behavior of SF10 specimens at a 5 MPa confining pressure and a  $10^{-5}/s$  strain rate is shown in Figure 10. The peak value (i.e., compressive strength) and initial slope (i.e., elastic modulus) of the specimen gradually decrease as the number of F–T cycles increases. The shape of the stress–strain curve also gradually changes. In comparison to the thaw–thaw specimen, the descending portion of the curve was shorter and steeper after 200 F–T cycles. As F–T cycling increases, the ability of the specimen to absorb energy decreases, as shown by the narrow area under the curve.

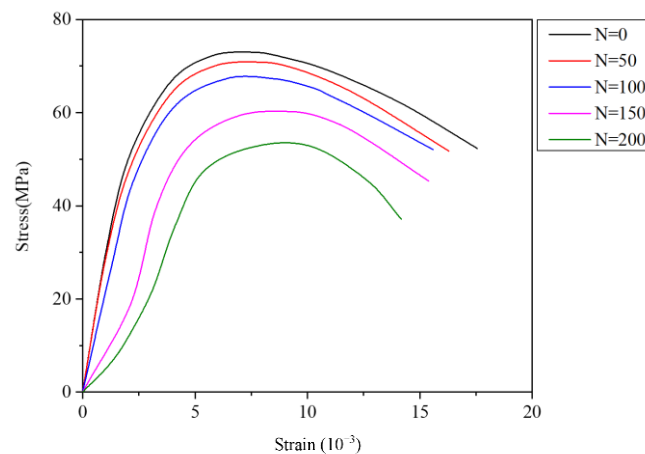


**Figure 10.** Stress–strain curve of SF10 specimens with 5 MPa confining pressure and  $10^{-5}$ /s strain rate under different numbers of F–T cycles.

The effect of different confining pressures on the stress–strain behavior of SF10 specimens at 100 F–T cycles and  $10^{-5}$ /s strain rates is shown in Figure 11. For the concrete specimens, the slope of the curve (i.e., elastic modulus) continues to increase as the confining pressure increases, and the stress–strain curve compaction stage becomes obvious. In addition, the energy absorption capacity increases significantly with the increase in confining pressure. This observation can be interpreted as the fact that confining pressure can inhibit the propagation of concrete cracks [45], thereby fundamentally improving the performance of concrete and increasing macroscopic characteristic parameters such as strength and elastic modulus.

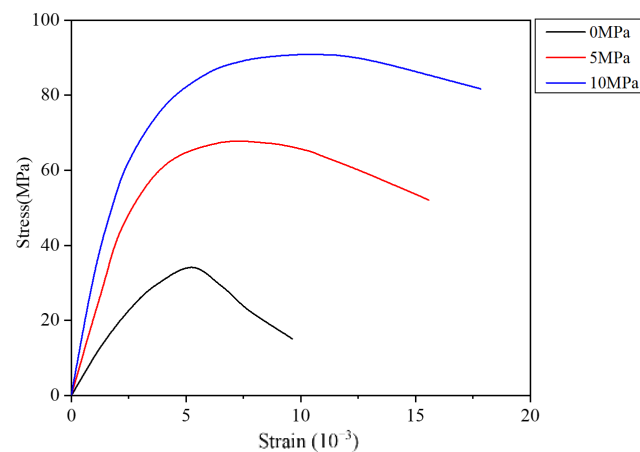


**Figure 11.** Stress–strain curve of SF10 specimens with 100 F–T cycles and  $10^{-5}$ /s strain rate under different confining pressures.

The influence of different strain rates on the stress–strain behavior of SF10 specimens at a 100 F–T cycle and a 5 MPa confining pressure is shown in Figure 12. The deformation of the SFRC specimen can be separated into four stages under quasi-static strain rate loading ( $10^{-5}$ /s): the pore compaction stage (AB1), elastic stage (B1C1), unstable cracking stage (C1D1) and subsequent failure stage. The AB1 stage reflects the closing process of the pores in concrete at the initial stage of loading, in which an upward concave shape is shown. The initial section of the stress–strain curve is approximately straight as the strain rate increases. The analytical object was chosen to be the strain rate of  $10^{-2}$ /s. Compared with the quasi-static strain rate, this value does not show the stage of pore compaction. The cause could be that at high strain rates, micro void in specimen has not been fully closed and then directly enters the elastic stage (AB2), in which the pores of concrete are further

compacted, and the relationship between stress and strain in specimen follows Hooke's law. The unstable cracking section (B2C2) occurs at this stage. Under high strain rate loading, the crack development speed in the specimen is accelerated, new cracks will appear, the damage degree of concrete is intensified the curve gradually convexes from the previous straight line section, and the slope is reduced. When the stress increases, the curve convexes from the previous straight line section. When it reaches the peak point, it will enter the stage of failure.

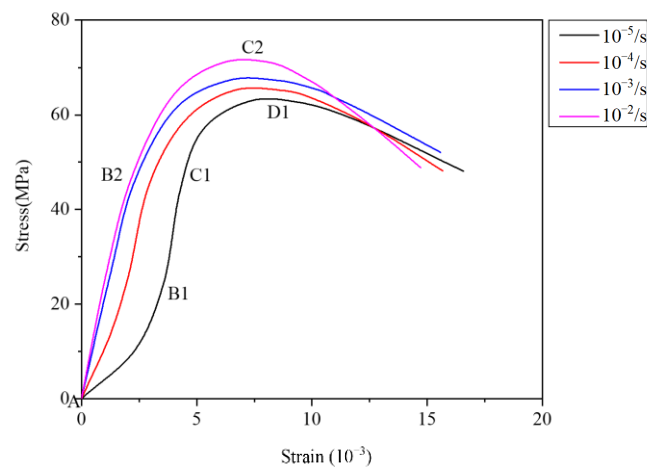


**Figure 12.** Stress–strain curve of SF10 specimens with 100 F–T cycles and 5 MPa confining pressure under different strain rates.

The influence of steel fiber content on the stress–strain behavior of concrete specimens is shown in Figure 13. The increase in peak stress, peak strain and area under the curve (energy dissipation capacity) for specimens with 1.0% and 2.0% steel fiber content in comparison to specimens without steel fibers, indicating that addition of steel fibers has a positive effect in the concrete. However, the reinforcement of the specimens containing 2.0% steel fibers was less effective than that of the specimens containing 1.0%. This phenomenon might be brought on by the overuse of steel fiber in concrete mixing, which makes it not easy to disperse evenly and agglomerate easily [43].

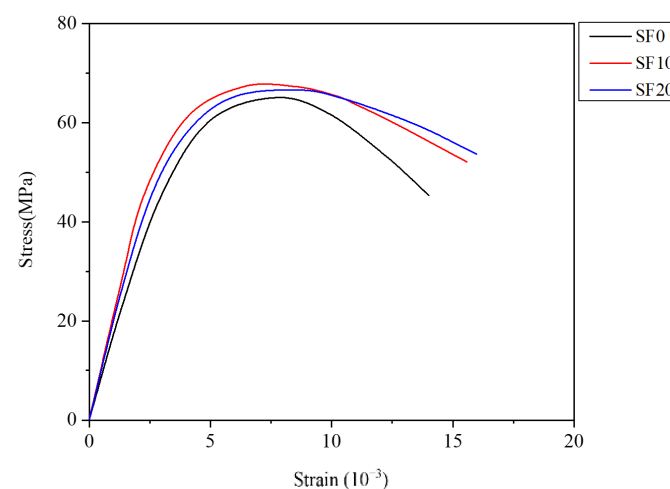


**Figure 13.** Stress–strain curve of different concrete specimens with 5 MPa confining pressure and  $10^{-5}/s$  strain rate under 100 F–T cycles.

### 3.4. Failure Mode

The failure modes of SF10 under different freeze–thaw cycles at a confining pressure of 5 MPa are shown in Figure 14. Obviously, the degree of damage to the SFRC surface

is affected by the F–T cycles, and as the F–T times grow, the slag on the concrete surface tends to get worse. Fuzzy cracks can be seen by triaxial compression testing when the concrete specimen is under 0 F–T cycles. The concrete specimen displayed a loose mortar after 50 F–T cycles, and mortar peeling was seen at the fractures. The loose mortar and shedding gradually increased with the times of F–T cycles. Due to the substantial amount of loose mortar present after 200 F–T cycles, the major crack in the specimen deepened, even though there was no change in the angle between the crack surface and the horizontal surface. Therefore, under the negative effect of F–T cycles, the failure mode of SFRC after triaxial compression did not change, but the width of inclined cracks gradually increased after specimen failure, because F–T cycling accelerated the internal damage of concrete specimens. It can be seen that SF10 remains as a whole after 200 freeze–thaw failures, so it can be concluded that the addition of fibers helps to strengthen the durability of the concrete.

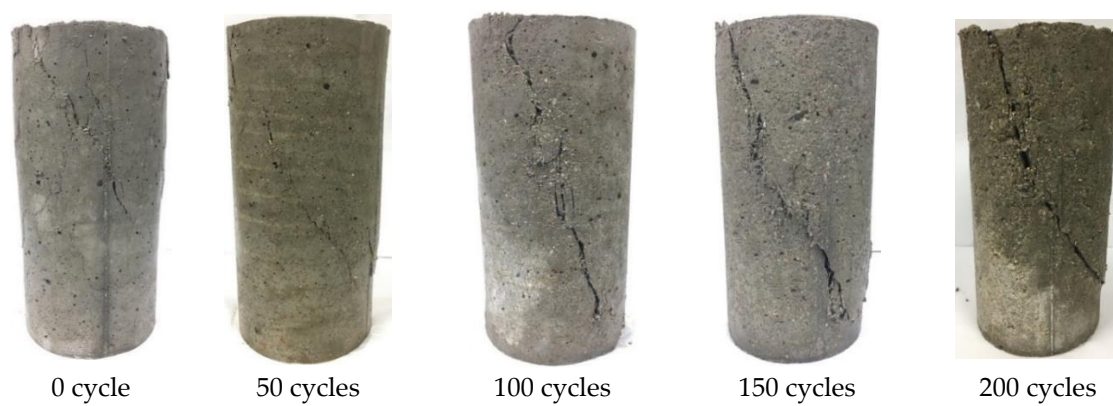


**Figure 14.** Failure mode of SF10 specimens with 5 MPa confining pressure under different numbers of F–T cycles.

Figure 15 displays the failure modes of SF10 under various strain rates at a confining pressure of 0 MPa. The failure mode of SFRC is almost independent of strain rate, a finding similar to that of Chen et al. [46]. Given the stress concentration at these interfaces and the existence of weak interface, microcracks readily propagate along the aggregate matrix interfaces and steel fiber matrix interfaces at a low strain rate. However, many of the coarse aggregates fractured and the sound was loud during the test with the strain rate increased. This may be due to the fracture becoming highly distributed at a relatively rapid strain rate, which prevents it from having enough time to choose the weakest failure interface and instead causes it to spread along the quickest path of energy release, i.e., directly through the aggregate [47,48]. Furthermore, the failure of the specimen tends to be severe as the strain rate increases. There are a number of studies that have yielded consistent results. Wang et al. [36] showed that as strain rate increases, the number of falling debris on the concrete surface increases gradually, and the surface with cracks became rough. In addition, high strain rate causes the specimen’s crack width to be wider than low strain rate does [49]. It can be seen that SF10 remains a whole after different strain rate failures, and almost does not form penetration cracks, so it can be concluded that the addition of fibers helps to enhance the bonding performance and durability of concrete.



**Figure 15.** Typical failure modes of SF10 specimen with 0 MPa confining pressure at different strain rates.

The failure modes of SFRC under confining pressures of 5 and 10 MPa are similar, and this result is the same as that from the study by Farnam et al. [50]. Therefore, Figure 16 illustrates the failure modes of SF0, SF10 and SF20 specimens at a strain rate of  $10^{-3}/s$  and confining pressures of 0 and 5 MPa. Obviously, the failure mode of SFRC has changed greatly due to lateral restraint pressure. Under 0 MPa confining pressure, the main cracks parallel to the direction of loading force appear on the surface of the plain concrete specimen when it reaches its ultimate compressive strength. The specimen subsequently fails as a result of a reduction in axial bearing capacity, demonstrating vertical splitting as the mode of failure (Figure 16a). The fracture surface was observed as a whole with good flatness and no adhesion. However, the cracks on the surface of specimen are localized in the center of the concrete and hardly any through cracks form when steel fiber is introduced. The fracture surface also shows the aggregate cement matrix connected by steel fiber, and the spalling degree in the middle part of the concrete is light and exhibits expansion because of the high content of steel fiber (the content is 2.0%). Jin et al. [1] reported extremely strong bond strengths between steel fibers and concrete, consistent with the results of the above studies. When cracks appear in the matrix, the steel fiber mesh connects the small pieces of concrete with its good bonding properties, thereby preventing the matrix from being crushed.

However, Figure 16b shows that under triaxial compression, confining pressure can effectively prevent vertical cracks, and the failure mode of the specimen changes to a typical oblique shear failure. This finding is close to previous results [46,51,52]. As shown in Figure 16b, the shear failure of plain concrete presents  $45^{\circ}$ – $50^{\circ}$  inclined cracks, and the width of the crack is large. During the test, the specimen cracks completely along the crack surface. Nevertheless, the diagonal shear crack widths started to narrow as a result of the joining action of the steel fibers in the SF10 and SF20 damaged specimens, which nonetheless displayed strong integrity. Under uniaxial and triaxial compression states, the failure modes for SFRC specimens are shown in Figure 17.



**Figure 16.** Typical failure modes of SFRC specimen under different confining pressures: (a) 0 and (b) 5 MPa.

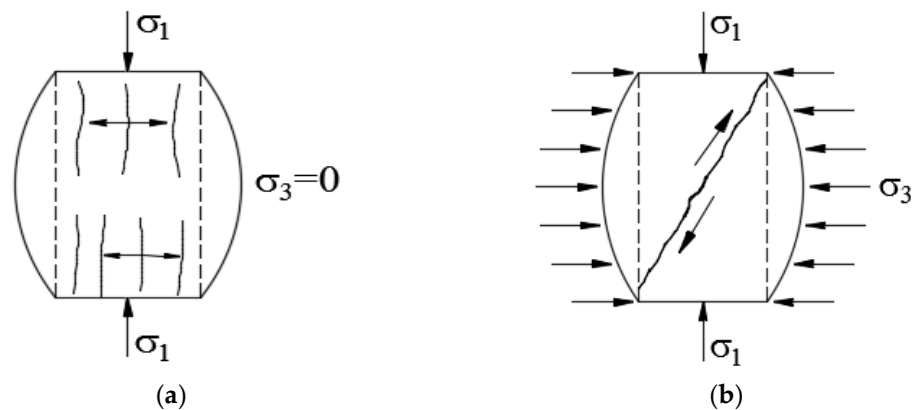


**Figure 17.** Model diagram of SFRC under different stress states. (a) Uniaxial compression state and (b) triaxial compression state.

### 3.5. DIF

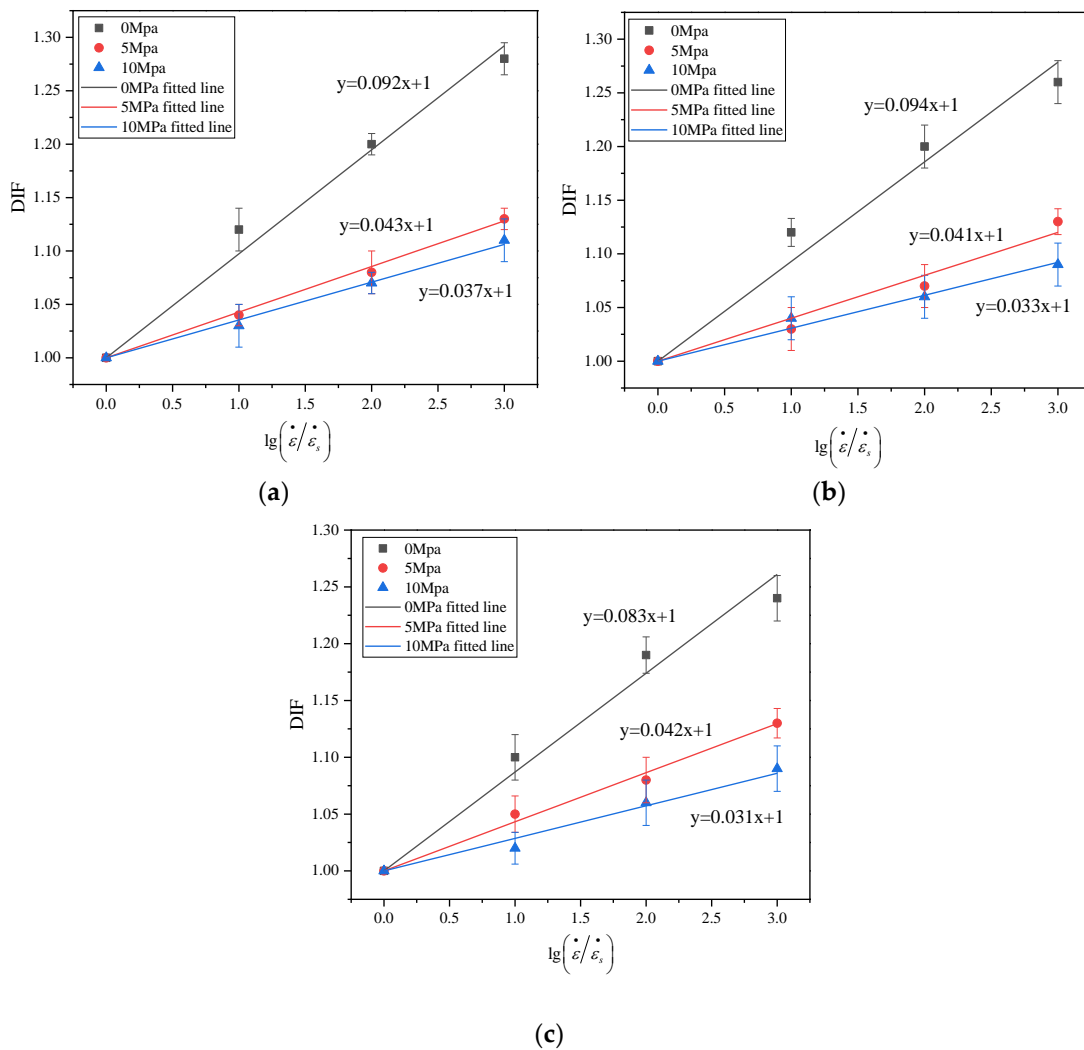
DIF is often used to quantitatively study the dynamic properties of materials, which can characterize the strength enhancement due to strain rate effects. The DIF is calculated as:

$$\text{DIF} = \frac{f_d}{f_s} = 1 + k \lg \left( \frac{\dot{\varepsilon}_d}{\dot{\varepsilon}_s} \right) \quad (1)$$

where  $f_d$  is the dynamic ultimate compressive strength,  $f_s$  is the quasi-static ultimate compressive strength,  $\dot{\varepsilon}_d$  is the current strain rate,  $\dot{\varepsilon}_s$  is the quasistatic strain rate ( $\dot{\varepsilon}_s = 1 \times 10^{-5}/\text{s}$ ) and  $k$  is a parameter.

Figure 18 shows the relationship between the dynamic ultimate compressive strength increment and the strain rate of concrete under different confining pressure levels after 100 F–T cycles. Table 5 shows the results of least squares fitting to the experimental data. With

the increases in strain rate, the DIF of the SFRC exhibits a linear increasing trend, and the slope of the fitted line decreases with increasing confining pressure, as shown clearly in Figure 18. This finding is accordant with an earlier study [25], but differs slightly from Wang et al. [37], who found that the DIF of concrete strength grows nonlinearly as increasing strain rate relation. The reason for this conflict is that the concrete samples are saturated with water prior to mechanical loading. As the concrete confining pressure increases, the sensitivity of the concrete ratio also increases [37]. Additionally, as the strain rate increases, the DIF growth rate of steel fiber reinforced concrete is slightly slower compared with control concrete. Therefore, the rate sensitivity of concrete strength decreases after adding a certain amount of steel fibers.

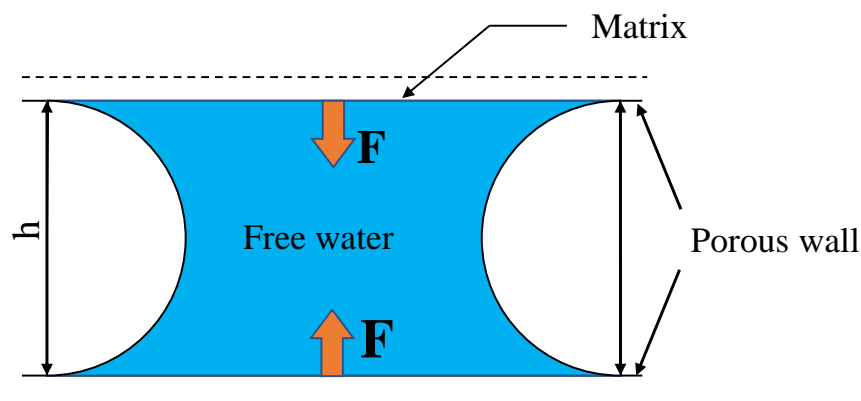


**Figure 18.** Relationship between DIF and strain rate of concrete subject to 100 F–T cycles under different confining pressure levels. (a) SF0, (b) SF10 and (c) SF20.

**Table 5.** Classification of  $\text{CaCO}_3$  produced by microorganisms and its suitable environmental conditions in concrete structures.

Specimens ID	Confining Pressure (MPa)	k	R <sup>2</sup>
SF0	0	0.0981	0.9813
	5	0.0430	0.9942
	10	0.0369	0.9912
SF10	0	0.0938	0.9604
	5	0.0406	0.9780
	10	0.0331	0.9868
SF20	0	0.0874	0.9813
	5	0.0433	0.9944
	10	0.0296	0.9795

In concrete, water is contained in pores of many different sizes. Similar to the Stefan effect, the water and concrete matrix can also be regarded as a system during dynamic loading. Hence, viscous resistance is generated as shown in Figure 19. This viscous effect also has an important influence on the sensitivity of the concrete ratio [53,54]. Steel fibers are distributed in a 3D manner in the specimen and thereby produce a supporting effect on the aggregate. In this way, the internal structure of concrete becomes compact, the porosity is reduced and the permeability is improved. In addition, the propagation of cracks inside the specimen was prevented and the damage to the concrete structure caused by the F–T cycle was reduced due to the crack resistance of the steel fibers. Therefore, under the action of F–T cycling, the porosity of SFRC is lower than that of plain concrete, indicating that the former has fewer micro-units of viscous resistance than the latter. The triaxial compressive strength of steel fiber concrete increases more slowly than that of control concrete, meaning that its sensitivity to the strain rate is lower than that of the control concrete.

**Figure 19.** Stefan effect of concrete pore water.

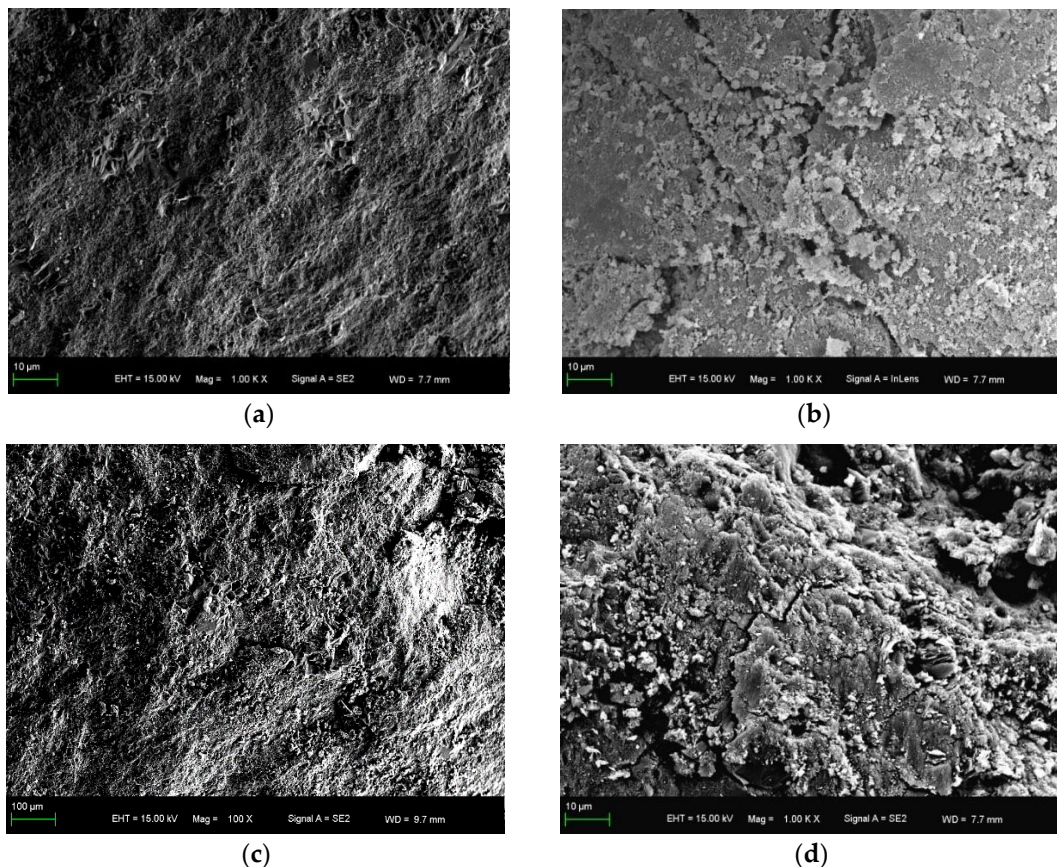
Furthermore, Zhang et al. [55] and Li et al. [56] made note of that there is also the relationship between the fracture toughness of rock-like materials and the strain rate, which reflects the material's capacity to limit crack propagation. The fracture toughness and resistance to crack growth both rise as the strain rate does. For microcell structures in concrete, each crack under dynamic loading creates additional resistance compared to static loading. Given the relatively small number of cracks in SFRC, the total additional resistance is also relatively small. As a result, the triaxial compressive strength of SFRC has a lower strain rate sensitivity than plain concrete.

### 3.6. Microstructure Analysis

The macro-mechanical properties of concrete largely depend on its micro-structure. Evaluation of degraded concrete microstructure provides valuable information that is applicable in many situations. The number and morphology of hydration products, the

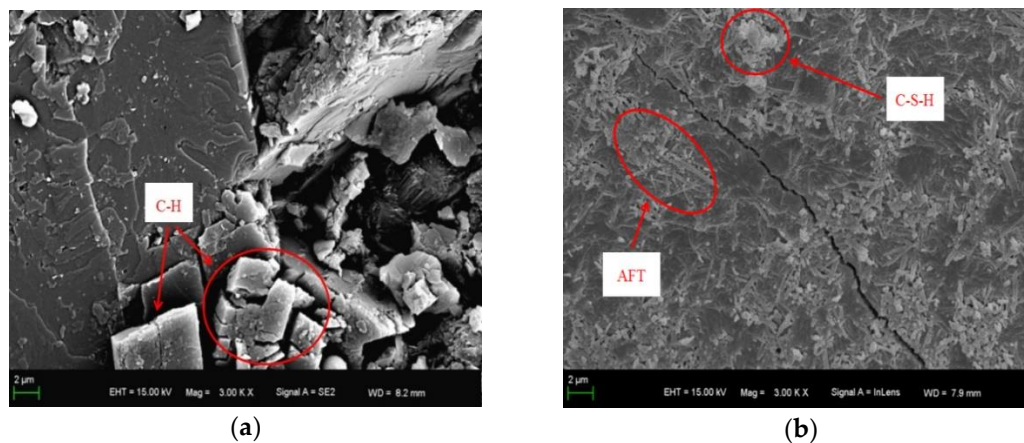
number of cracks and holes in the SFRC matrix, aggregate–matrix interface transition zone (ITZ) and steel fiber–matrix ITZ were studied to further understand the degradation mechanism of SFRC under F–T cycle.

Figure 20 shows the SEM images of different samples under different F–T cycles. The surface of the SF0 specimen without a F–T cycle is dense and free of cracks, as shown in Figure 20a. After 200 F–T cycles, damage can be observed, i.e., the surface becomes rough with numerous microcracks and pores (Figure 20b). Figure 20c,d show that the SF10 specimen has a similar trend to the SF0 specimen. This finding provides a good explanation for the reduction in concrete compressive strength due to microstructural damage.



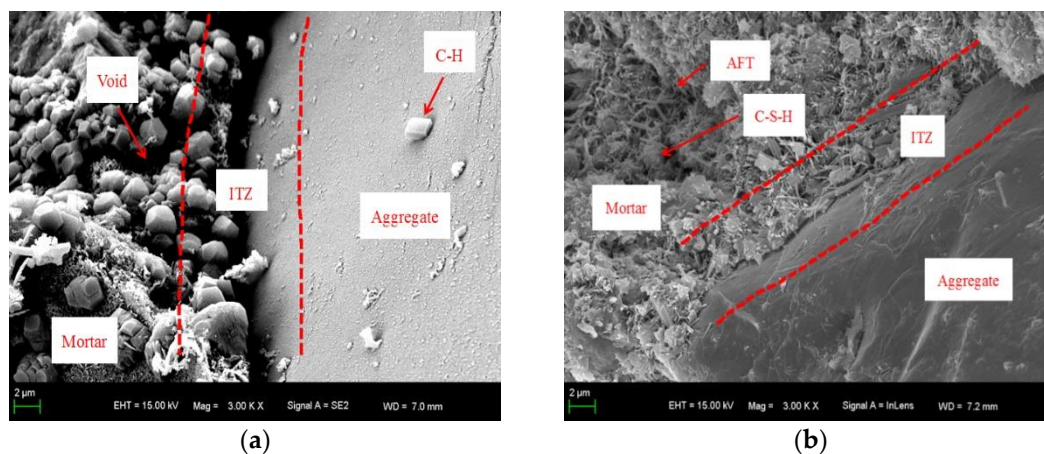
**Figure 20.** SEM images of specimen under a different number of F–T cycles: (a) SF0 with 0 F–T cycles, (b) SF0 with 200 F–T cycles, (c) SF10 with 0 F–T cycles and (d) SF10 with 200 F–T cycles.

Figure 21 shows the microstructure of the SFRC matrix. It can be seen that a greater number of calcium hydroxide (C–H) exists in plain concrete matrix, and the amounts of hydrated calcium silicate (C–S–H) and Ettringite (AFT) are relatively small. Many micro cracks and holes can be found, and the structure is relatively loose (Figure 21a). However, the amounts of AFT and C–S–H in SF10 matrix are relatively large, and only a few of C–H are distributed around AFT (Figure 21b). Good structure compactness is also observed. Therefore, the addition of steel fibers improves the density and microstructure of concrete. Additionally, the strength and deformation properties of concrete are improved due to the network structure formed by steel fiber which can bridge the cracks.



**Figure 21.** Micromorphology of matrix. (a) SF0 and (b) SF10.

The ITZ of aggregate and matrix microstructure is shown in Figure 22. Cracks and voids and many hexagonal plate-like C–H are found in the ITZ of aggregate and matrix for plain concrete, and the AFT is loose. However, the mortar and aggregate in SFRC are fully bonded because of the random distribution of steel fiber, and the width of the crack between the aggregate and matrix is reduced. The amount of C–H decreases due to the addition of steel fiber. Orientation also changed accordingly, which has an important influence on improving the micro morphology of aggregate and matrix interface. The honeycomb-like C–S–H and needle-like AFT cover the cracks and the surface of the voids, thereby making the concrete a dense and uniform continuum. Under external load, the compactness of the structure delays the formation of cracks in the interface transition area; hence, the strength of concrete increases accordingly [57,58].



**Figure 22.** Micromorphology of ITZ of aggregate and matrix. (a) SF0 and (b) SF10.

Figure 23 shows the ITZ micromorphology between the steel fibers and the matrix of the SF10 specimen. The interface between the steel fibers and the matrix exhibits a height difference and a certain bonding effect. This may be due to the increased surface roughness of steel fibers after collision with the aggregate during concrete mixing, and the surface damage of steel fiber can improve the friction and bonding performance between steel fiber and mortar [59]. However, many initial microcracks and holes are formed due to the incorporation of steel fiber; hence, the structure becomes loose [60]. The massive C–H gels (Figure 23b) found on the AFT surface hinder the continuous growth of AFT and negatively affect the interface performance of cement-based concrete to some extent.

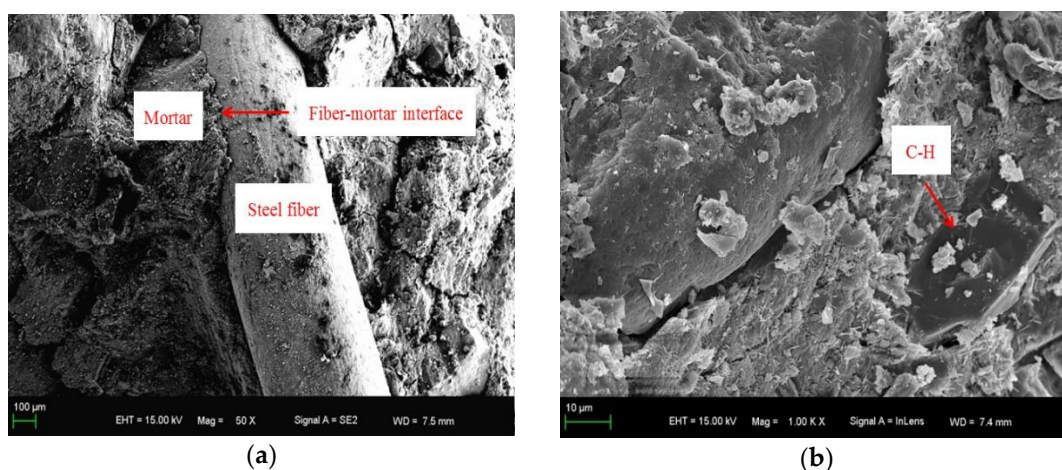


**Figure 23.** Micromorphology of ITZ between steel fiber and matrix of SF10 specimen. (a) ITZ micromorphology and (b) C–H gels.

#### 4. Conclusions

Research has been conducted on concrete with varying steel fiber contents under F–T cycles to systematically examine the effects of confining pressure and strain rate on dynamic mechanical properties. Based on the research results, the following conclusions are drawn:

- (1) With increasing F–T cycles, the triaxial compressive strength of concrete specimens declines, the stress–strain curve area decreases with time, and the corresponding energy absorption capacity gradually weakens. However, the failure mode of the concrete did not change, only the deterioration of the specimen gradually increased.
- (2) The F–T damage of SFRC shows two stages: (I) from 0 to 50 F–T cycles, the compressive strength of specimens slowly decreases and the peak strain slowly increases; and (II) from 50 to 200 F–T cycles, the compressive strength and peak strain of specimens acceleratingly decreases and increases, respectively. Similarly, mortar shedding and crack extension on the specimen surface were also accelerated in the second stage.
- (3) Under F–T cycles, steel fiber can enhance the dynamic mechanical properties of concrete. Adding steel fibers to concrete under F–T cycles increases the triaxial compressive strength, peak strain, and energy absorption capacity. However, increasing steel fiber content to 2.0%, the triaxial compressive strength of concrete decreases because the excessive steel fiber causes a small amount of agglomeration.
- (4) As the strain rate increases, the compressive strength of the SFRC subjected to F–T cycles increases gradually, the peak strain decreases slowly and the DIF of strength increases linearly. In low strain rate, SFRC specimens have sufficient time to select the path, most of which are along the mortar interior or the weak surface of aggregate mortar. However, when the strain rate increases, the shape of failure surface of the SFRC changes and a large number of coarse aggregate fractures occur.
- (5) Under F–T cycles, specimens with no confining pressure exhibit crack directions parallel to loading stress directions, and the cracks are concentrated in the middle of the specimen. However, the steel fiber reinforced concrete specimens change to inclined shear failure under the action of confining pressure. In addition, as confining pressure increased under F–T cycling, SFRC's triaxial compressive strength increased as well as its peak strain and energy absorption capacity.
- (6) The SEM tests conducted on concrete specimens after the F–T cycles show that steel fibers enhance the ITZ between aggregates and mortars, compaction and microstructure improvement of concrete. The microstructure analysis results are accordant with the laws of macroscopic properties (compressive strength and peak strain).

**Author Contributions:** Conceptualization, Y.L. (Yang Li); methodology, Y.L. (Yang Li) and Q.Z.; validation, Q.Z., Y.L. (Yang Li) and R.W.; formal analysis, Y.L. (Yang Li) and Q.Z.; investigation, Y.L. (Yang Li) and X.X.; resources, Y.L. (Yang Li) and Q.Z.; data curation, Q.Z. and R.W.; writing—original draft preparation, Y.L. (Yang Li) and Q.Z.; writing—review and editing, Y.L. (Yang Li) and J.W.; supervision, R.W. All authors have read and agreed to the published version of the manuscript.

**Funding:** This study was financially supported by Project funded by China Postdoctoral Science Foundation (program no. 2020M683687XB; 2022T150525); the National Natural Science Foundation of China (program no. 52009110; 51879217); Natural Science Basic Research Program of Shaanxi (program no. 2021JM-331); Young Talent Fund of Association for Science and Technology in Shaanxi, China (program no. 20220416), and Young Talent fund of Association for Science and Technology in Xi'an City (program no. 095920211332).

**Data Availability Statement:** Not applicable.

**Conflicts of Interest:** The authors declare no conflict of interest.

## References

1. Jin, L.; Zhang, R.B.; Tian, Y.D.; Dou, G.Q.; Du, X.L. Experimental investigation on static and dynamic mechanical properties of steel fiber reinforced ultra-high-strength concretes. *Constr. Build. Mater.* **2018**, *178*, 102–111. [\[CrossRef\]](#)
2. Yoo, D.Y.; Banthia, N. Mechanical and structural behaviors of ultra-high-performance fiber-reinforced concrete subjected to impact and blast. *Constr. Build. Mater.* **2017**, *149*, 416–431. [\[CrossRef\]](#)
3. Chen, M.; Chen, W.; Zhong, H.; Chi, D.; Wang, Y.H.; Zhang, M.Z. Experimental study on dynamic compressive behaviour of recycled tyre polymer fibre reinforced concrete. *Cem. Concr. Compos.* **2019**, *98*, 95–112. [\[CrossRef\]](#)
4. Hao, Y.; Hao, H.; Chen, G. Experimental investigation of the behaviour of spiral steel fibre reinforced concrete beams subjected to drop-weight impact loads. *Mater. Struct.* **2016**, *49*, 353–370. [\[CrossRef\]](#)
5. Vairagade, V.S.; Kene, K.S. Strength of normal concrete using metallic and synthetic fibres. *Procedia Eng.* **2013**, *51*, 132–140. [\[CrossRef\]](#)
6. Abbass, W.; Khan, M.I.; Mourad, S. Evaluation of mechanical properties of steel fiber reinforced concrete with different strengths of concrete. *Constr. Build. Mater.* **2018**, *168*, 556–569. [\[CrossRef\]](#)
7. Wang, Z.L.; Wu, J.; Wang, J.G. Experimental and numerical analysis on effect of fibre aspect ratio on mechanical properties of SRFC. *Constr. Build. Mater.* **2010**, *24*, 559–565. [\[CrossRef\]](#)
8. Farhan, N.A.; Sheikh, M.N.; Hadi, M.N.S. Behaviour of Ambient Cured Steel Fibre Reinforced Geopolymer Concrete Columns under Axial and Flexural Loads. *Structures* **2018**, *15*, 184–195. [\[CrossRef\]](#)
9. Yoo, D.Y.; Yoon, Y.S.; Banthia, N. Predicting the post-cracking behavior of normal- and high-strength steel-fiber-reinforced concrete beams. *Constr. Build. Mater.* **2015**, *93*, 477–485. [\[CrossRef\]](#)
10. Yang, D.P.; Zhang, B.; Liu, G.J. Experimental Study on Spall Resistance of Steel-Fiber Reinforced Concrete Slab Subjected to Explosion. *Int. J. Concr. Struct. Mater.* **2021**, *15*, 23. [\[CrossRef\]](#)
11. Domski, J.; Katzer, J. Comprehensive approach to evaluation of mechanical properties of waste aggregate concrete reinforced by steel fiber. *Tech. Pap.* **2018**, *2*, 75–453. [\[CrossRef\]](#)
12. Kantar, E.; Yuen, T.Y.P.; Kobya, V.; Kuang, J.S. Impact dynamics and energy dissipation capacity of fibre-reinforced self-compacting concrete plates. *Constr. Build. Mater.* **2017**, *138*, 383–397. [\[CrossRef\]](#)
13. Farhan, N.A.; Sheikh, M.N.; Hadi, M.N.S. Engineering Properties of Ambient Cured Alkali-Activated Fly Ash–Slag Concrete Reinforced with Different Types of Steel Fiber. *J. Mater. Civ. Eng.* **2018**, *30*, 04018142. [\[CrossRef\]](#)
14. Su, Y.; Li, J.; Wu, C.Q.; Wu, P.T.; Li, Z.X. Effects of steel fibres on dynamic strength of UHPC. *Constr. Build. Mater.* **2016**, *114*, 708–718. [\[CrossRef\]](#)
15. Zhang, P.; Zhen, G.; Wang, J.; Guo, J.J.; Wang, T.Y. Influencing factors analysis and optimized prediction model for rheology and flowability of nano-SiO<sub>2</sub> and PVA fiber reinforced alkali-activated composites. *J. Clean. Prod.* **2022**, *366*, 132988. [\[CrossRef\]](#)
16. Wu, H.; Ren, G.M.; Fang, Q.; Liu, J.Z. Effects of steel fiber content and type on dynamic tensile mechanical properties of UHPCC. *Constr. Build. Mater.* **2018**, *173*, 251–261. [\[CrossRef\]](#)
17. Zhang, P.; Han, X.; Hu, S.W.; Wang, J.; Wang, T.Y. High-temperature behavior of polyvinyl alcohol fiber-reinforced metakaolin/fly ash-based geopolymer mortar. *Compos. Part B Eng.* **2022**, *244*, 110171. [\[CrossRef\]](#)
18. Fang, Q.; Zhang, J. Three-dimensional modelling of steel fiber reinforced concrete material under intense dynamic loading. *Constr. Build. Mater.* **2013**, *44*, 118–132. [\[CrossRef\]](#)
19. Zhang, P.; Wang, W.S.; Lv, Y.J.; Wang, K.X.; Dai, S.Y. Effect of polymer coatings on the freezing–thawing and carbonation resistances of nano-SiO<sub>2</sub> and polyvinyl alcohol fiber-reinforced cementitious composites. *J. Mater. Res. Technol.* **2022**, *21*, 69–83. [\[CrossRef\]](#)
20. Ren, G.M.; Wu, H.; Fang, Q.; Liu, J.Z. Effects of steel fiber content and type on dynamic compressive mechanical properties of UHPCC. *Constr. Build. Mater.* **2018**, *164*, 29–43. [\[CrossRef\]](#)

21. Lu, X.B.; Thoms, H.C.T. Behavior of high strength concrete with and without steel fiber reinforcement in triaxial compression. *Cem. Concr. Res.* **2006**, *36*, 1679–1685. [[CrossRef](#)]
22. Li, Y.; Zhou, Y.; Wang, R.J. Experimental investigation on the properties of the interface between RCC layers subjected to early-age frost damage. *Cem. Concr. Compos.* **2022**, *134*, 104745. [[CrossRef](#)]
23. Noori, A.; Shekarchi, M.; Moradian, M.; Moosavi, M. Behavior of steel fiber-reinforced cementitious mortar and high-performance concrete in triaxial loading. *ACI Mater. J.* **2015**, *112*, 95–103. [[CrossRef](#)]
24. Foltz, R.R.; Lee, D.H.; LaFave, J.M. Biaxial behavior of high-performance fiber-reinforced cementitious composite plates. *Constr. Build. Mater.* **2017**, *143*, 501–514. [[CrossRef](#)]
25. Bao, J.W.; Wang, L.C.; Zhang, Q.Y.; Liang, Y.Q.; Jiang, P.Q.; Song, Y.P. Combined effects of steel fiber and strain rate on the biaxial compressive behavior of concrete. *Constr. Build. Mater.* **2018**, *187*, 394–405. [[CrossRef](#)]
26. Liu, D.X.; Xu, W.N.; Cheng, Z.L.; Zhou, Z.J.; Cai, X.Y.; Zhao, B.Q. Improvement test on frost resistance of vegetation-concrete and engineering application of test fruitage. *Environ. Earth Sci.* **2013**, *69*, 161–170.
27. Zhang, W.M.; Chen, S.H.; Zhang, N.; Zhou, Y. Low-velocity flexural impact response of steel fiber reinforced concrete subjected to freeze–thaw cycles in NaCl solution. *Constr. Build. Mater.* **2015**, *101*, 522–526. [[CrossRef](#)]
28. Li, L.; Zhang, Y.; Shi, Y. Surface Cracking and Fractal Characteristics of Cement Paste after Exposure to High Temperatures. *Fractal Fract.* **2022**, *6*, 465. [[CrossRef](#)]
29. Miao, C.W.; Mu, R.; Tian, Q.; Sun, W. Effect of sulfate solution on the frost resistance of concrete with and without steel fiber reinforcement. *Cem. Concr. Res.* **2002**, *32*, 31–34. [[CrossRef](#)]
30. Niu, D.T.; Jinag, L.; Bai, M.; Miao, Y.Y. Study of the performance of steel fiber reinforced concrete to water and salt freezing condition. *Constr. Build. Mater.* **2013**, *44*, 267–273. [[CrossRef](#)]
31. Wang, R.J.; Hu, Z.Y.; Li, Y.; Wang, K.; Zhang, H. Review on the deterioration and approaches to enhance the durability of concrete in the freeze–thaw environment. *Constr. Build. Mater.* **2022**, *321*, 126371. [[CrossRef](#)]
32. GB 175–2007; Common Portland Cements. General Administration of Quality Supervision, Inspection and Quarantine of the People’s Republic of China and Standardization Administration of the People’s Republic of China: Beijing, China, 2008.
33. CECS 13: 2009; Standard Test Methods for Fiber Reinforced Concrete. Chinese Association for Engineering Construction Standardization: Beijing, China, 2009.
34. GB/T 50082–2009; Standard for Long Term Durability Test Method of Ordinary Concrete. Ministry of Housing and Urban Rural Development of the People’s Republic of China: Beijing, China, 2009.
35. Lu, J.Z.; Zhu, K.F.; Tian, L.Z.; Guo, L. Dynamic compressive strength of concrete damaged by fatigue loading and freeze-thaw cycling. *Constr. Build. Mater.* **2017**, *152*, 847–855. [[CrossRef](#)]
36. Wang, Q.F.; Liu, Y.H.; Peng, G. Effect of water pressure on mechanical behavior of concrete under dynamic compression state. *Constr. Build. Mater.* **2016**, *125*, 501–509. [[CrossRef](#)]
37. Wang, H.; Wang, L.C.; Song, Y.P.; Wang, J.Z. Influence of free water on dynamic behavior of dam concrete under biaxial compression. *Constr. Build. Mater.* **2016**, *112*, 222–231. [[CrossRef](#)]
38. Reinhardt, H.W.; Cornelissen, H.A.W.; Hordijk, D.A. Tensile tests and failure analysis of concrete. *J. Struct. Eng.* **1986**, *112*, 2462–2477. [[CrossRef](#)]
39. Rossi, P.; Boulay, C. Influence of free-water in concrete on the cracking process. *Mag. Concr. Res.* **1990**, *42*, 143–146. [[CrossRef](#)]
40. Rossi, P. Influence of cracking in the presence of free water on the mechanical behaviour of concrete. *Mag. Concr. Res.* **1991**, *43*, 53–57. [[CrossRef](#)]
41. Rossi, P.; Vanmier, J.G.M.; Toutlemonde, F.; Le Maou, F.; Boulay, C. Effect of loading rate on the strength of concrete subjected to uniaxial tension. *Mater. Struct.* **1994**, *169*, 260–264. [[CrossRef](#)]
42. Kytinou, V.K.; Chalioris, C.E.; Karayannis, C.G. Analysis of Residual Flexural Stiffness of Steel Fiber Reinforced Concrete Beams with Steel Reinforcement. *Materials* **2020**, *13*, 2698. [[CrossRef](#)]
43. Emmanuel, E.A.; Messaoud, S.; Adegoke, O.O.; Mark, T. Effect of mix design methods on the mechanical properties of steel fibre-reinforced concrete prepared with recycled aggregates from precast waste. *Structures* **2020**, *27*, 664–672.
44. Wang, R.J.; Zhang, Q.J.; Li, Y. Deterioration of concrete under the coupling effects of freeze–thaw cycles and other actions: A review. *Constr. Build. Mater.* **2022**, *319*, 126045. [[CrossRef](#)]
45. Fu, Q.; Xu, W.R.; Li, D.; Li, N.; Niu, D.T.; Zhang, L.; Guo, B.B.; Zhang, Y.L. Dynamic compressive behaviour of hybrid basalt-polypropylene fibre-reinforced concrete under confining pressure: Experimental characterisation and strength criterion. *Cem. Concr. Compos.* **2021**, *118*, 103954. [[CrossRef](#)]
46. Chen, Z.; Hu, Y.; Li, Q.B.; Sun, M.Y.; Lu, P.Y.; Liu, T.Y. Behavior of concrete in water subjected to dynamic triaxial compression. *J. Eng. Mech.* **2010**, *136*, 379–389. [[CrossRef](#)]
47. Xiao, J.Z.; Li, L.; Shen, L.M.; Poon, C.S. Compressive behaviour of recycled aggregate concrete under impact loading. *Cem. Concr. Res.* **2015**, *71*, 46–55. [[CrossRef](#)]
48. Li, L.; Poon, C.S.; Xiao, J.Z.; Xuan, D.X. Effect of carbonated recycled coarse aggregate on the dynamic compressive behavior of recycled aggregate concrete. *Constr. Build. Mater.* **2017**, *151*, 52–62. [[CrossRef](#)]
49. Xiao, J.Z.; Li, L.; Shen, L.M.; Yuan, J.Q. Effects of strain rate on mechanical behavior of modeled recycled aggregate concrete under uniaxial compression. *Constr. Build. Mater.* **2015**, *93*, 214–222. [[CrossRef](#)]

50. Guler, S.; Akbulut, Z.F. Residual strength and toughness properties of 3D, 4D and 5D steel fiber-reinforced concrete exposed to high temperatures. *Constr. Build. Mater.* **2022**, *327*, 126945. [[CrossRef](#)]
51. Chen, Y.L.; Chen, Z.P.; Xu, J.J.; Liu, E.M.; Wu, B. Performance evaluation of recycled aggregate concrete under multiaxial compression. *Constr. Build. Mater.* **2019**, *229*, 116935. [[CrossRef](#)]
52. Wang, L.P.; Li, N.; Qi, J.L.; Tian, Y.Z.; Xu, S.H. A study on the physical index change and triaxial compression test of intact hard rock subjected to freeze–thaw cycles. *Cold Reg. Sci. Technol.* **2019**, *160*, 39–47.
53. Kaplan, S.A. Factors affecting the relationship between rate of loading and measured compressive strength of concrete. *Mag. Concr. Res.* **1980**, *32*, 79–88. [[CrossRef](#)]
54. Rossi, P.; Toutlemonde, F. Effect of loading rate on the tensile behaviour of concrete: Description of the physical mechanisms. *Mater. Struct.* **1996**, *29*, 116–118. [[CrossRef](#)]
55. Zhang, Z.X.; Kou, S.Q.; Yu, J.; Yu, Y.; Jiang, L.G.; Lindqvist, P.A. Effects of loading rate on rock fracture. *Int. J. Rock Mech. Min. Sci.* **1999**, *36*, 597–611. [[CrossRef](#)]
56. Li, H.B.; Zhao, J.; Li, T.J. Micromechanical modelling of the mechanical properties of a granite under dynamic uniaxial compressive loads. *Int. J. Rock Mech. Min. Sci.* **2000**, *37*, 923–935. [[CrossRef](#)]
57. Li, J.J.; Niu, J.G.; Wan, C.J.; Jin, B.; Yin, Y.L. Investigation on mechanical properties and microstructure of high performance polypropylene fiber reinforced lightweight aggregate concrete. *Constr. Build. Mater.* **2016**, *118*, 27–35. [[CrossRef](#)]
58. Wang, R.J.; Yu, N.N.; Li, Y. Methods for improving the microstructure of recycled concrete aggregate: A review. *Constr. Build. Mater.* **2020**, *242*, 118164. [[CrossRef](#)]
59. Lerch, J.O.; Bester, H.L.; Van Rooyen, A.S.; Combrinck, R.; Villiers, W.I.; Boshoff, W.P. The effect of mixing on the performance of macro synthetic fiber reinforced concrete. *Cem. Concr. Res.* **2018**, *103*, 130–139. [[CrossRef](#)]
60. Wen, C.C.; Zhang, P.; Wang, J.; Hu, S.W. Influence of fibers on the mechanical properties and durability of ultra-high-performance concrete: A review. *J. Build. Eng.* **2022**, *52*, 104370. [[CrossRef](#)]